SUBCONTRACT TITLE**:** **Fabrication and Physics of CdTe Devices by Sputtering**

SUBCONTRACT TITLE**:** **ZXL-5-44205-01**

QUARTERLY TECHNICAL STATUS REPORT FOR**:**
Phase 3/Quarter 1

SUBMITTED TO**:** **Bolko von Roedern**
National Renewable Energy Laboratory

PRINCIPAL INVESTIGATORS:

A.D. Compaan, R.W. Collins, V.G. Karpov
Department of Physics and Astronomy
Dean Giolando
Dept. of Chemistry
2801 W Bancroft,
Toledo, OH 43606

This progress report covers the First Quarter of Phase 3 for the period from June 1, 2007 through August 31, 2007, of the above Thin Film Photovoltaic Partnership Program subcontract.
In this report we highlight 1) spectroscopic ellipsometry measurements of the optical constants of ultra-thin films of sputtered CdTe and CdS, 2) optical properties of gold nanocrystals studied as a possible route to enhancing the optical coupling of light in ultra-thin II-VI semiconductor films, and 3) a theory of admittance spectroscopy for thin films with resistive electrodes.

1. Optical Properties of Ultra-Thin CdTe and CdS Films

In this quarter, the effort in real time and *ex situ* optical analysis by spectroscopic ellipsometry has focused on the properties of ultrathin CdTe and CdS films, and Au nanostructures. The motivation of these studies is two-fold. First a better understanding of the evolution of initial stage film optical properties and grain structure is sought for CdS and CdTe as it relates to the optimization of the film deposition process for solar cell performance. Second, the CdS/CdTe/Cu/Au system is a good candidate for nanostructured third generation PV devices, and it is of interest to characterize the thin layer properties in order to identify appropriate structures for such applications. Additional detail on these motivations will be clarified as the data and analysis results are presented.

CdTe and CdS thin films were magnetron sputtered onto ultra-smooth, native-oxide-covered, single-crystal Si wafers, using the deposition parameters shown in Table 1.1. The substrate temperatures and the growth rates are obtained by analyzing the real-time spectroscopic ellipsometry (RTSE) data collected *in situ* during film growth (as described in previous reports). For both CdTe and CdS films, RTSE data analysis yields a typical surface roughness layer thickness (d_s) evolution with bulk layer thickness (d_b) as shown in Fig. 1.1. Three distinct regions are observed:

(1) cluster formation during initial nucleation (roughening peak) followed by cluster coalescence (smoothening);

(2) stabilization of the surface roughness layer;

(3) long term evolution of significant roughness.

The study reported here is focused on region (2), where both the clustering/coalescence effect and the surface roughening effect on the optical properties of the film can be minimized. With the deposition parameters in Table 1.1, d_b in this stable surface region is sufficiently small so that quantum confinement effects may occur, and the extent of this region is wide enough in thickness to permit observation of the evolution of such effects with film thickness -- without the added complication of surface roughness development. In fact, the surface roughness remains within the range of 12-15 Å over the bulk layer thickness range from 50 to 250 Å for the CdTe deposition of Fig. 1.1.

Table 1.1: Deposition parameters for magnetron sputtered CdTe and CdS thin films.

	Substrate temperature (°C)	**rf power (Watt)**	**Ar pressure/flow (mTorr/sccm)**	**growth rate (Å/sec)**
CdTe	188	60	18/23	0.79
CdS	229	50	10/23	0.47

The optical properties of the ultrathin CdTe and CdS films are obtained by exact inversion of the measured ellipsometric angles (ψ, Δ) in order to extract the complex dielectric functions $\varepsilon = \varepsilon_1 + i\varepsilon_2$, using the known (i) angle of incidence (AOI), (ii) substrate structure and optical properties (measured before the onset of deposition), and (iii) film thicknesses (d_b and d_s) as deduced from the RTSE data. This approach works acceptably well for CdTe, but not as well for CdS. In the latter case, there is an apparent artifact in the inversion result when d_b is small (see Fig. 1.2). Because this artifact occurs where the crystalline Si substrate exhibits strongly varying optical properties, we attribute this problem to damage to the substrate interface region by

incident ions which modify the Si substrate optical properties from those obtained before the onset of deposition. This effect was simulated by adding an interface layer just below the native oxide with the optical properties of amorphous silicon (a-Si). The a-Si simulates the damge due to ion bombardment which is expected to be larger for CdS due to the lower pressure and also due to S which has a lower mass and can penetrate more deeply into the substrate in the

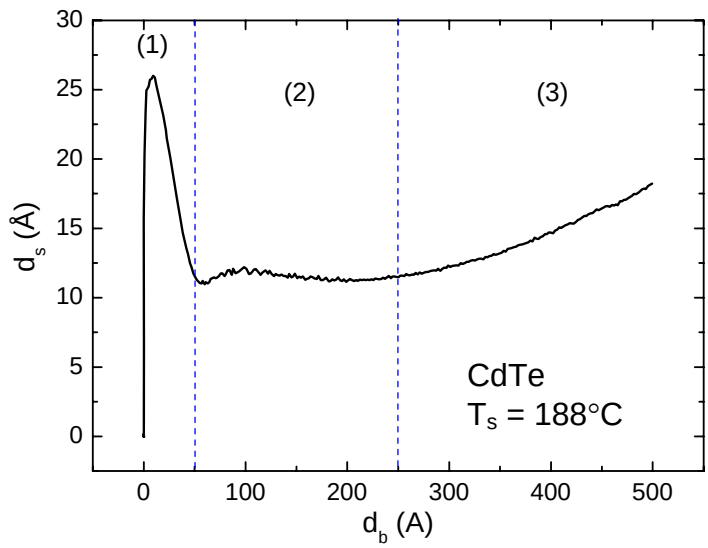

Figure 1.1: Typical surface roughness layer thickness evolution with bulk layer thickness observed for both CdTe and CdS, deduced in an analysis of RTSE data. Three distinct regions are marked: (1) nucleation/coalescence (d_b < 50 Å); (2) stable surface region (50 Å < d_b < 250 Å); and (3) gradual long term roughening (d_b > 250 Å).

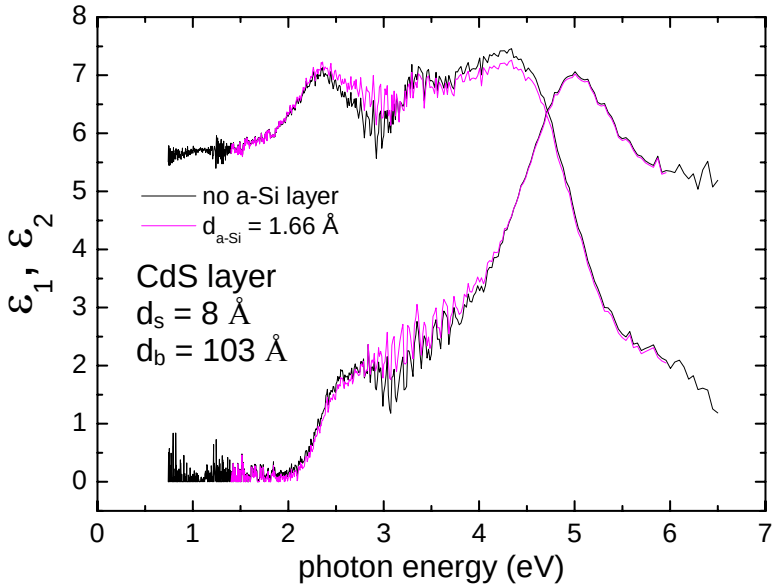

Figure 1.2: Comparison of the inverted dielectric function of a CdS film with and without an interface layer to simulate ion bombardment damage at the substrate interface.

initial stages of CdS film growth. In principle, both the damage layer thickness d_i and the a-Si volume fraction f_a can be deduced from the RTSE data; however, for simplicity, the volume fraction was set at 1. Although d_i was found to be quite small (~ 1 monolayer), the existence of such an interface layer can reduce the artifact in the inversion results (see Fig. 1.2). Another possible contribution to the artifact is intrinsic stress that can change the amplitudes and positions of the dielectric function features of the deposited CdS film in the interface region relative to that in the bulk; however, such an effect cannot fully account for the nature of the artifact.

Ultra-thin CdTe film

Figure 1.3 shows the dielectric function of the CdTe film at several values of the effective thickness $d_{eff} = d_b + (d_s/2)$, a quantity that describes the total amount of deposited material including both bulk and surface roughness layers. It can be seen that the optical properties undergo continuous changes in the thickness range of 50-250 Å, especially at the E_1 critical point (CP). To quantify these changes, the dielectric functions were fit to an analytical model based on the parabolic band approximation: [1]

$$\varepsilon = \sum_n A_n \exp(i\phi_n)\,(E_n - E - i\Gamma_n)^{\mu_n} \qquad (1)$$

where A_n, ϕ_n, E_n, Γ_n, and μ_n are the amplitude, phase, resonance energy, width, and exponent of the nth CP respectively.

The best fit parameters are shown in Figure 1.4 as functions of effective thickness. From an inspection of Fig. 1.3, the E_1 CP undergoes the largest variation with d_{eff} -- in

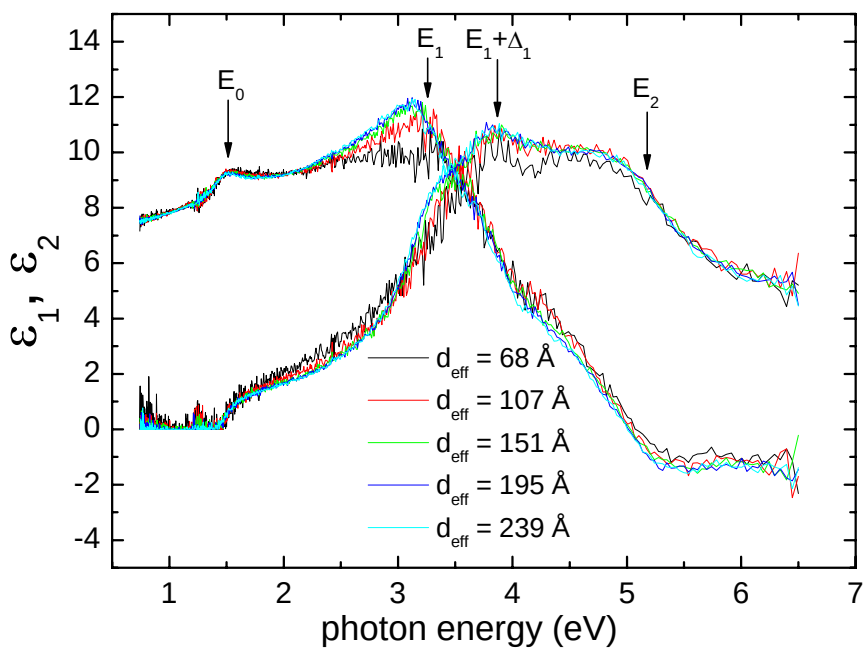

Figure 1.3: Complex dielectric functions of a magnetron sputtered CdTe thin film at five effective thicknesses, with deposition parameters shown in Table 1.1.

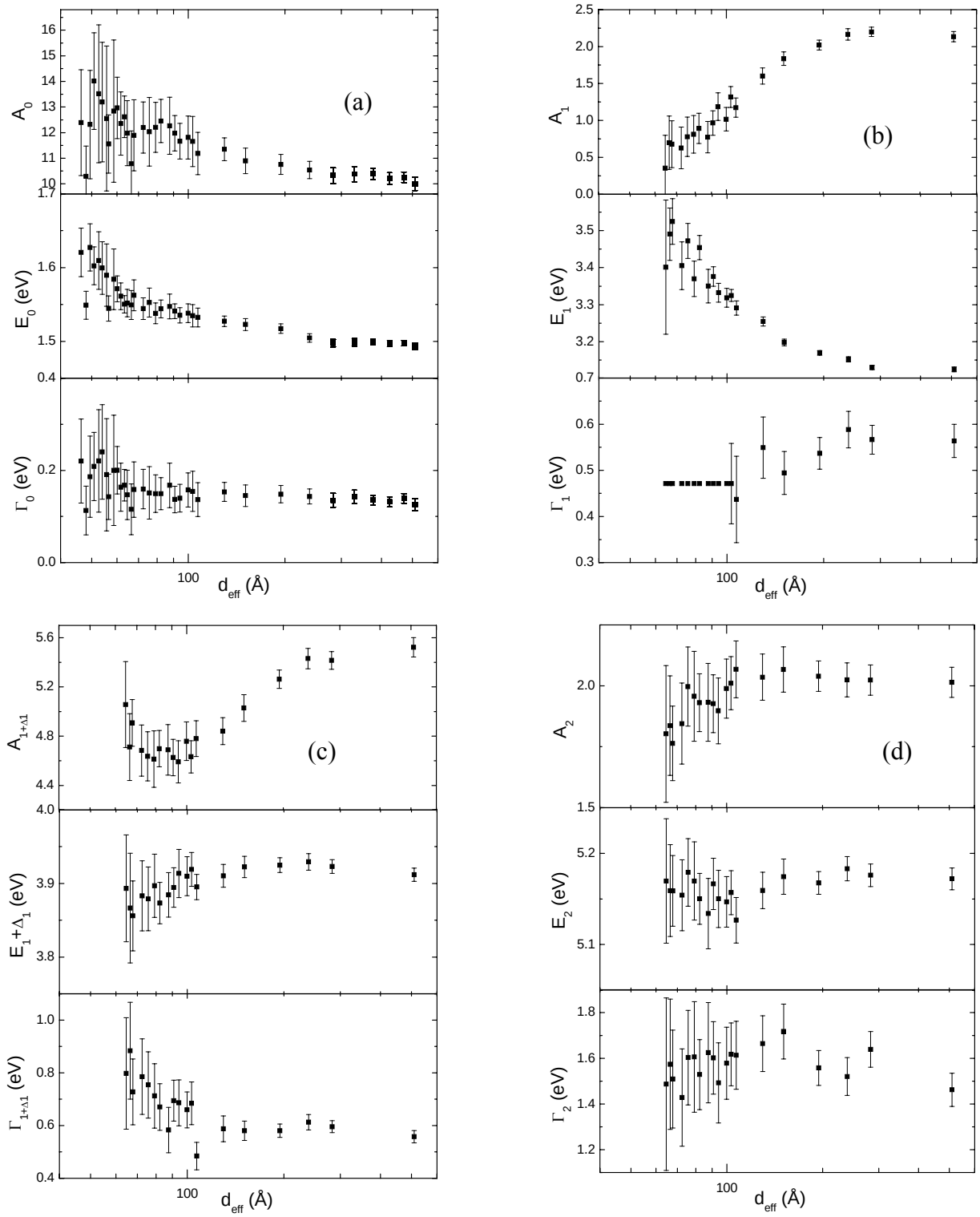

Figure 1.4: The critical point amplitudes, resonance energies, and width parameters for the (a) E_0, (b) E_1, (c) $E_1+\Delta_1$, and (d) E_2 CPs of a CdTe thin film as functions of the total effective film thickness. The error bars indicate the 90% confidence limits.

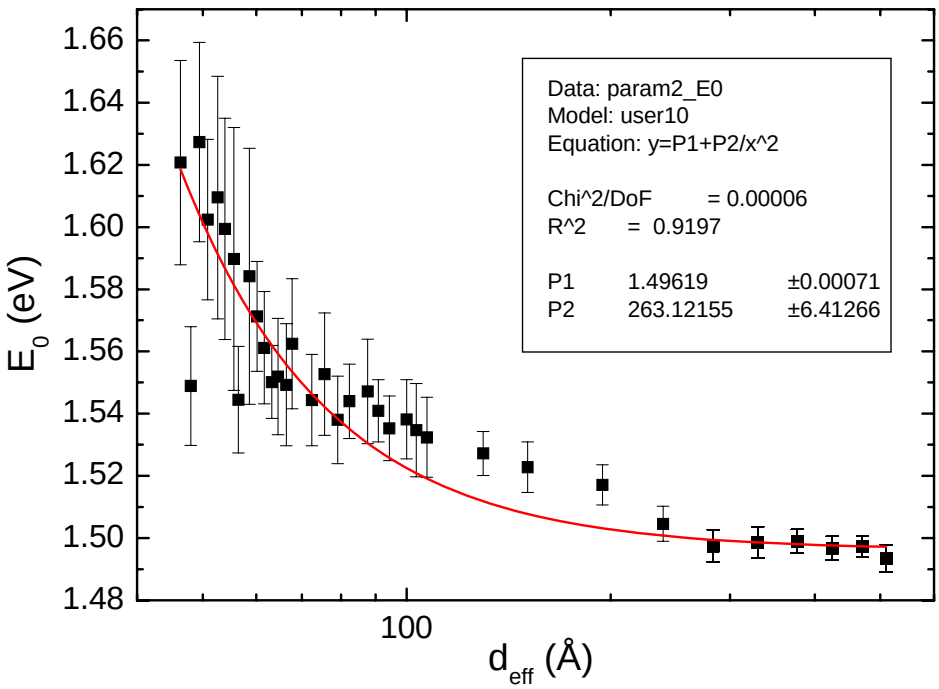

Figure 1.5: Fit to the E_0 vs. d_{eff} curve for the CdTe film, using equation 2.

both its amplitude and resonance energy. This CP becomes weaker as the film becomes thinner [see the top panel of Fig. 1.4 (b)]. At $d_{eff} \sim 68$ Å, this CP effectively disappears (considering the confidence limits in A_1); this can also be observed directly in the data of Fig. 1.3 as a flattening in ε_1 around 3 eV and an approach to linearity in ε_2 above 3 eV. Because this CP becomes so weak for $d_{eff} < 100$ Å, its broadening parameter Γ_1 must be fixed at the value obtained at $d_{eff} = 100$ Å for the lowest thicknesses [see the bottom panel of Fig. 1.4(b)], otherwise the fitting program will fail.

The resonance energy of the E_0 CP, also known as the fundamental gap E_g, is the key parameter for optoelectronic properties and particularly for solar cell structures. E_g undergoes a significant blue shift as the film becomes thinner as observed in the center panel of Fig. 1.4 (a). This blue shift is even stronger for the E_1 resonance energy as observed in the center panel of Fig. 1.4 (b). The well known "particle in a box" model can be used to explain such shifts, assuming in the case of the E_0 transition that the electrons at the bottom of conduction band can be approximated as free electrons with effective mass m_e*. This may be appropriate as the size of the box approaches the Bohr radius of the exciton given by $a_B = a_0 \varepsilon m_e/\mu$, where $a_0 = 0.529$ Å is the Bohr radius for H atom, μ is the reduced effective mass, ε is the low frequency dielectric constant. Using values for CdTe of $\mu \sim 0.09 m_e$ and $\varepsilon \sim 7.5$, then a_B(CdTe) ~ 44 Å; then the excitons are likely to become unstable in the small thickness range of this study and the free electron approximation may be valid. Considering that the film has just coalesced from isolated clusters, it is reasonable to assume that the shape of each grain is columnar with height d_{eff} and cross-sectional area L^2, where L is the average distance between two nuclei which evolve into the grains. Assuming each grain can be modeled as a 3D infinite potential well, then one can derive:

$$E_0 = E_0^b + (\hbar^2\pi^2/2m_e^*)\,[2/L^2 + 1/d_{eff}^2] \qquad (2)$$

where E_0^b is the E_0 value in bulk CdTe. The reductions in the amplitudes of higher energy critical points with decreasing thickness may be an indication that void structures are trapped between the grains in the very thin film regime, even after coalescence, thus justifying the three-dimensional confinement model of Eq. (2).

Equation (2) was used to fit the E_0 vs. d_{eff} data in Figure 1.4 (a), as shown in Fig. 1.5. In the fit of Fig. 1.5, greater weight was given to the points with the narrower confidence limits. From this fit and from Eq. (2), the appropriate effective mass was determined to be $m_e^* \sim (0.143 \pm 0.003)\ m_e$, which is close to the value of 0.11 m_e found previously.[2] It should be kept in mind that all measurements were performed in real time, and thus, all band gaps in Fig. 1.5 are appropriate for the deposition temperature of 188°C. Applying the bulk value for the temperature shift of the band gap for CdTe, $dE_g/dT \sim 3.7 \times 10^{-4}$ eV/°C, room temperature (20°C) band gaps of 1.56 eV and 1.68 eV are estimated respectively for the bulk-like CdTe film and for the 50 Å thick CdTe film of Fig. 1.5. The wider band gap for the bulk film compared to the single crystal value (1.49 eV) is attributed to stress which is greatest in films deposited at low temperature. In fact, a larger stress closer to the substrate interface can account for the deviations of the data in Fig. 1.5 from the best fit using Eq. (2). Although the E_0 transition can be understood with a simple confinement model, understanding the clear trends in the E_1 energy and amplitude and the much weaker trends in the $E_1+\Delta_1$ and E_2 parameters must await band structure calculations.

Finally, considering the CP widths, these values are nearly constant within the error bars over the thickness range of 100-500 Å for all CPs. This an indication that the grain size remains constant with thickness over this range, so that coarsening of the microstructure does not occur with thickness. Increases in the broadening parameter with decreasing thickness may occur at lower thicknesses; however, it is unclear whether this is an effect of the grain structure or the electronic structure.

Ultra-thin CdS film

Figure 1.6 shows the inverted dielectric functions of the CdS film at four d_{eff} values, where $d_{eff} = d_b + (d_s/2)$. Compared to Fig. 1.3, it can be observed that the variation in the CdS E_0 energy with thickness is much weaker than those of CdTe E_0 and E_1 over the corresponding thickness range. This can be explained, at least in part, by the larger electron and hole effective masses in CdS as tabulated in Ref. 3. Furthermore, if one calculates the exciton Bohr radius (using $m_e^*=0.2m_e$ and $m_h^*=0.7m_e$ and $\varepsilon \sim 5.5$ for CdS), a value of $a_B(\text{CdS}) \sim 19$ Å is obtained. Thus, the free electron approximation must be replaced by free exciton model for the quantum confinement. Because our previous work has shown that the intrinsic stress in the CdS films is significantly larger than that of the CdTe film, variations in the stress with thickness, rather than an electronic confinement effects, may dominate the weak variation of the CdS E_0 critical point energy. Unfortunately, the two CPs E_1-A and E_1-B, are so close to each other and so broadened at this deposition temperature and in the thin layers that it is impossible to resolve them in parameterizing the dielectric functions. So in this work, the focus is on the narrow energy range around the E_0 CP.

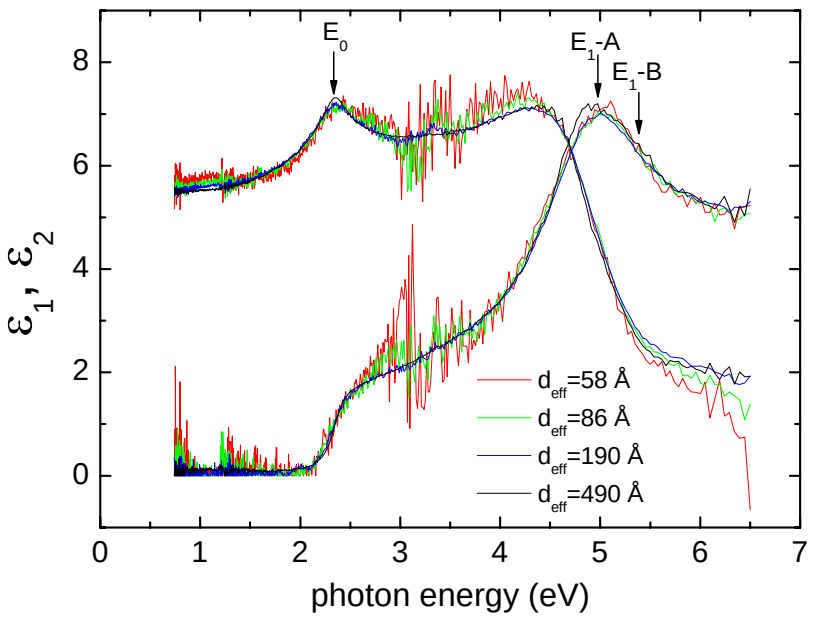

Figure 1.6: Complex dielectric functions of a magnetron sputtered CdS thin film at five effective thicknesses; the deposition parameters are given in Table 1.1.

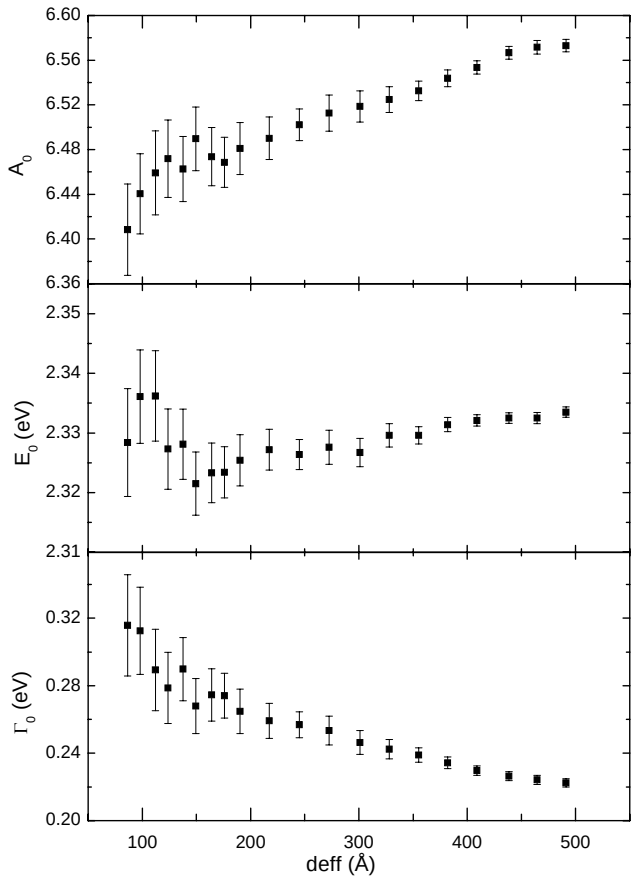

Fig. 1.7: E_0 CP parameters (amplitude, energy, width) of the CdS thin film as a function of d_{eff}.

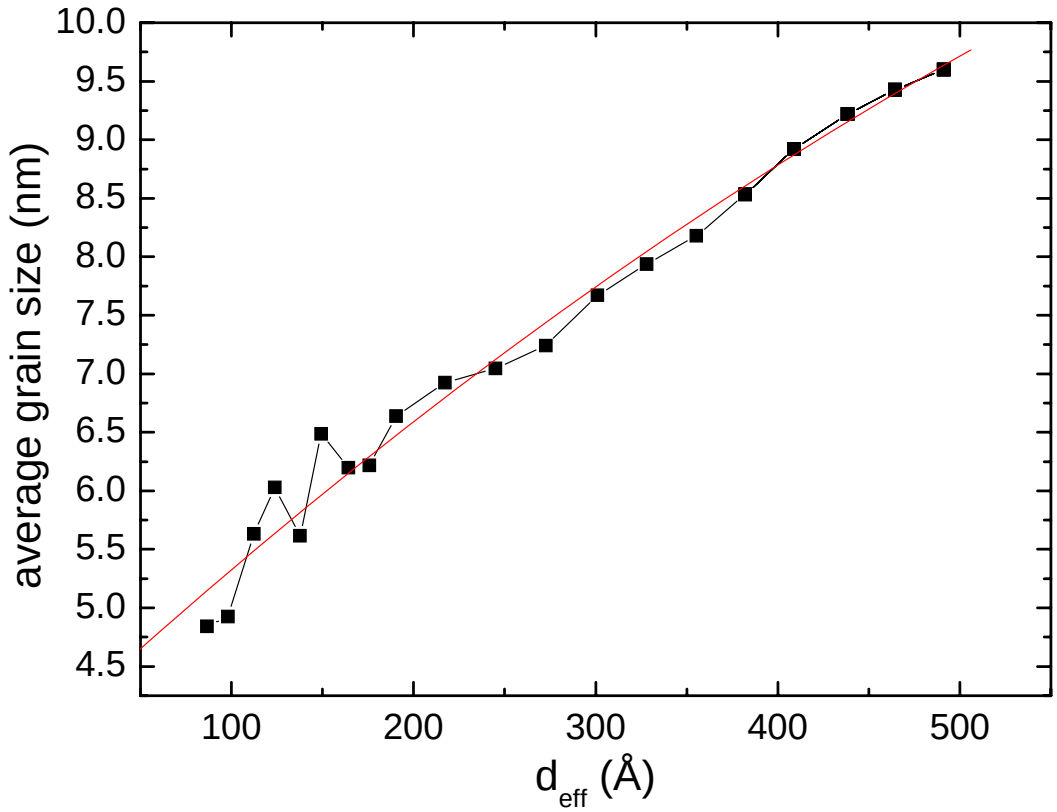

Figure 1.8: Estimated average grain size in the CdS thin film as a function of d_{eff}.

The E_0 CP parameters are shown in Fig. 1.7. The weak variation in E_0 may be due to a combination of exciton confinement at the lowest thicknesses and an increase in stress with thickness at the largest thickness. However, the latter effect seems counter-intuitive to the extent that the continuous decrease of Γ_0 with increasing d_{eff} indicates that the average grain size increases as the film grows (within this thickness range). Such grain growth would be expected to relax the stress with increasing thickness. Thus, the origin of the weakly increasing band gap in Fig. 1.7 is unclear – possibly it is related to a reduction in defects (that give a lower energy absorption tail) as the grain size increases. Based on our previously reported model, the average grain size can be estimated as a function of d_{eff}, by using a excited carrier group velocity for each CP. The final results are shown in Fig. 1.8. The thickness variation of the grain size for CdS in this figure is significantly different than the essentially constant grain size with thickness for CdTe. This difference in behavior may reflect differences in grain evolution – e.g., conical structures for CdS versus columnar structures for CdTe – or in the re-nucleation behavior. Finally, the evolution of A_0 for CdS must be considered in view of the variation in Γ_0. When the exponent is not unity, A_0 does not represent the oscillator strength, and this parameter may vary along with Γ_0 to ensure a constant oscillator strength.

2. Optical Properties of Au Nanocrystals

Gold (Au) nanocrystals provide a means for making contact to CdS/CdTe nanostructures, and can also be used for plasmon optical enhancement in traditional thin film CdTe solar cells. In this study, films consisting of gold (Au) nanocrystals surrounded by an alkanethiol, $C_{12}SH$, have been deposited (by T. Bigioni, Univ. Toledo) on fused silica and native oxide covered crystalline silicon substrates, as shown by the transmission electron microscopy (TEM) image in Figure 1.9. The $C_{12}SH$ layer is designed to prevent coalescence of the Au nanocrystals on the substrate surface, as depicted in the illustration of Figure 1.9. The TEM image indicates that the spherical nanocrystals are 6 nm in diameter and form a close-packed hexagonal array. The interparticle spacing is ~8 nm due to a 1.5 nm shell of self-assembled $C_{12}SH$ molecules attached to the nanocrystals. Room temperature ellipsometric spectra in (ψ, Δ) were collected ex situ at four angles of incidence, Θ_I = 45°, 55°, 65°, and 75°, using a variable-angle rotating-compensator multichannel spectroscopic ellipsometer[4,5] over the spectral range from 0.75 to 5.0 eV. Normal incidence transmittance data for the film on fused silica were also collected using this instrument.

For the Au nanocrystal film prepared on a native-oxide-covered crystalline silicon wafer, the dielectric function spectra (ε_1, ε_2) and film thickness (d_b) (Au nanocrystal thickness and its surrounding $C_{12}SH$ shell) and the underlying native oxide thickness (d_{ox}) were extracted using a least squares regression analysis with an unweighted error function[6], an initial dielectric function parameterization, and a four-medium optical model consisting of (semi-infinite crystalline silicon substrate)/(native oxide)/film/(air ambient). From the Au nanocrystal film thickness (d_b) and the native oxide thickness

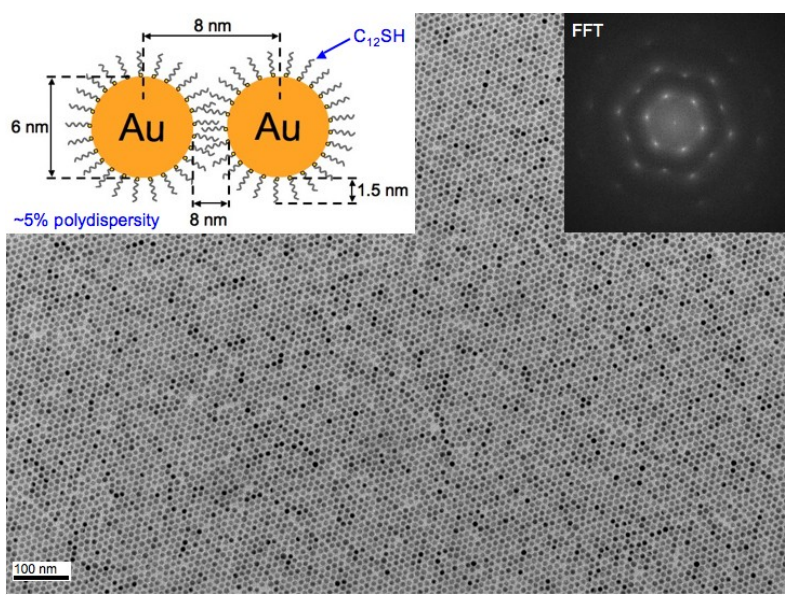

Figure 1.9: Transmission electron microscopy (TEM) image for a Au nanocrystal film where the nanocrystals are separated by $C_{12}SH$. Also shown are diffraction patterns and illustrations for this material.

(d_{ox}), a numerical inversion procedure[7] is then used to extract the dielectric function spectra for the Au nanocrystal layer exactly. The dielectric function spectra from numerical inversion were then parameterized anew using an improved optical model consisting of three Tauc-Lorentz oscillators[8,9] sharing a common Tauc gap and a constant additive term to ε_1 represented by ε_∞. Each Tauc-Lorentz oscillator can be described by:

$$\varepsilon_2 = \begin{cases} \dfrac{AE_0\Gamma}{\left(E^2 - E_0^2\right)^2 + \Gamma^2 E^2} \dfrac{\left(E - E_g\right)^2}{E} & E > E_g \\ 0 & E \le E_g \end{cases},$$

and (Eq. 3)

$$\varepsilon_1 = \frac{2}{\pi} P \int_{E_g}^{\infty} \frac{\xi \varepsilon_2(\xi)}{\xi^2 - E^2} d\xi,$$

with energy independent parameters consisting of an amplitude A, a broadening parameter Γ, a resonance energy E_0, and a common Tauc gap E_g.

Figure 1.10 depicts the dielectric function spectra for the Au nanocrystal film extracted using the numerical inversion, as well as the best parameterization of these dielectric functions using a three Tauc-Lorentz oscillator model. The energy-independent parameters and film thickness are given in Table 1.2. By comparing the dielectric functions for the Au nanocrystal film with those of bulk Au material[10], it can be seen that the nanocrystal film exhibits a particle plasmon resonance at ~2.06 eV in the ε_2 spectra, which is represented by the lowest resonance oscillator in the parameterization. Furthermore, the higher energy features in the (ε_1, ε_2) spectra are present for both the Au nanocrystal and bulk films, indicating that the lower amplitude of the features for the nanocrystal film can be attributed to a lower density of Au in the film as compared to the bulk material. It should also be noted that the film thickness extracted by spectroscopic ellipsometry, d_b = 7.549 nm, is in precise agreement with the diameter of the Au nanocrystals at ~6 nm, including the ~1.5 nm $C_{12}SH$ at the top of the film depicted in the TEM image in Figure 1.9. The native oxide layer thickness on the Si substrate, d_{ox} = 6.26 nm, is higher than values generally observed on similar substrates (d_{ox} ~ 2 nm). This difference can be attributed to the fact that the layer of $C_{12}SH$ on the underside of the nanocrystals is difficult to distinguish optically from the SiO_2 native oxide layer (both with index of refraction n~1.45-1.50 at the plasmon resonance). Thus, the underside $C_{12}SH$ layer is interpreted within the optical model as part of the SiO_2 layer. In fact the 6.26 nm oxide layer suggests that there may be more than one such alkanethiol monolayer at the substrate interface, or alternatively, the oxide on the silicon wafer increased in thickness (by 4 nm) during nanocrystal film growth and processing.

The analysis of the Au nanocrystal film deposited on glass was carried out in a similar manner, although the similarity between the optical properties of $C_{12}SH$ and the bulk substrate required a different initial model to determine the nanocrystal film thickness, d_b. The film thickness (d_b) was once again extracted using a least squares regression analysis with an unweighted error function and a three-medium optical model consisting of (semi-infinite glass substrate)/film/(air ambient). In this instance, the (ε_1, ε_2) spectra obtained from the analysis of the Au nanocrystal film on native-oxide-covered crystalline silicon were used as reference spectra in the fitting procedure. After the film thickness was determined and fixed using the

previously described model, numerical inversion was used to extract the exact dielectric function spectra for the Au nanocrystal

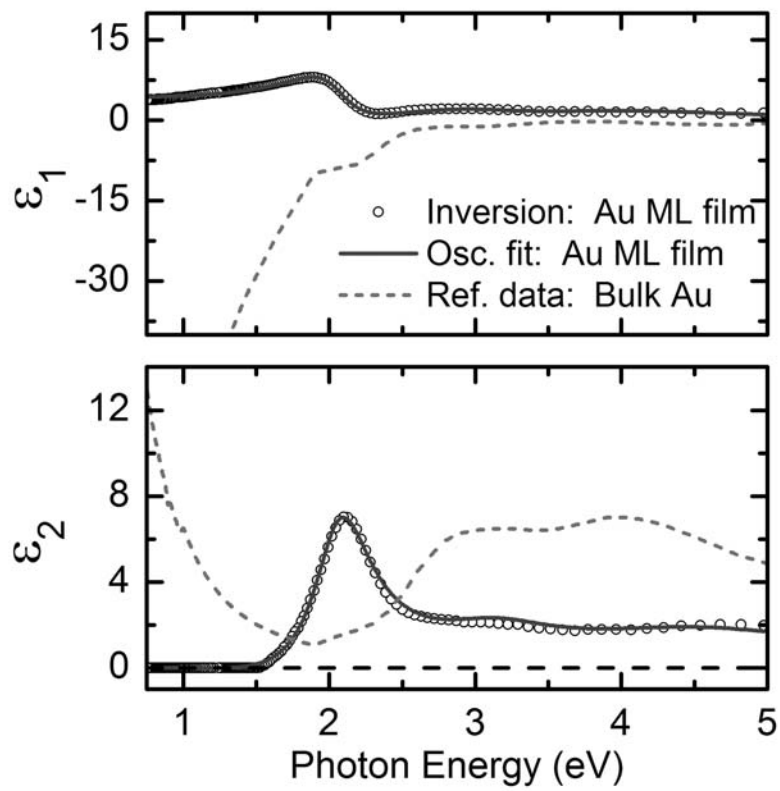

Figure 1.10: Dielectric function spectra (ε_1, ε_2) for the Au nanocrystal film prepared on native-oxide-covered crystalline silicon determined from numerical inversion (open circles), parameterized fit to inversion data from Table 1.2 (solid line), and bulk Au (dashed line) all over the spectral range from 0.75 to 5.0 eV.

Table 1.2: Energy-independent parameters describing the three Tauc-Lorentz oscillator model used to fit the (ε_1, ε_2) spectra obtained from artifact minimization and numerical inversion for the Au nanocrystal film on native oxide covered crystalline silicon. Also shown are the native oxide thickness (d_{ox}) and the bulk film thickness (d_b) determined from initial parameterization of the ellipsometric spectra in (ψ, Δ), as well as the unweighted estimator, σ, from the parameterization of the dielectric function spectra.

D_b = 7.549 ± 0.18 nm **d_{ox} = 6.263 ± 0.161 nm** **σ = 0.2039**

E_0 (eV)	**Γ (eV)**	**A (eV)**	**E_g (eV)**	**ε_∞**
2.063±0.00181	0.48506±0.00846	22.891±0.514	1.2845±0.465	1.8366±0.0594
3.1455±0.0348	1.0092±0.17	3.2295±0.872	-	-
4.6675±0.106	2.5208±0.485	7.3453±2.37	-	-

layer on glass. The dielectric function spectra from numerical inversion were once again parameterized using an optical model consisting of three Lorentz oscillators and a constant additive term to ε_1 represented by ε_∞.

Figure 1.11 depicts the dielectric function spectra for the Au nanocrystal film on fused silica extracted using numerical inversion, as well as the parameterization of these dielectric functions using a three Tauc-Lorentz oscillator model. The energy-independent parameters and film thickness are given in Table 1.3. The optical properties of this film are remarkably similar to the film prepared on native oxide covered crystalline silicon, and exhibit the same similarity to bulk Au material at high energy, but with a particle plasmon resonance at ~2.2 eV in the ε_2 spectra, which is represented by the lowest resonance oscillator in the parameterization. Once again the film thickness extracted by spectroscopic ellipsometry, d_b = 7.23 nm, is in good agreement with the diameter of the Au nanocrystals at ~6 nm surrounded by ~1.5 nm $C_{12}SH$ depicted in the TEM image in Figure 1.9. The somewhat lower energy of the plasmon in the case of the c-Si substrate can be attributed to greater screening of the plasmon resonance by the substrate.

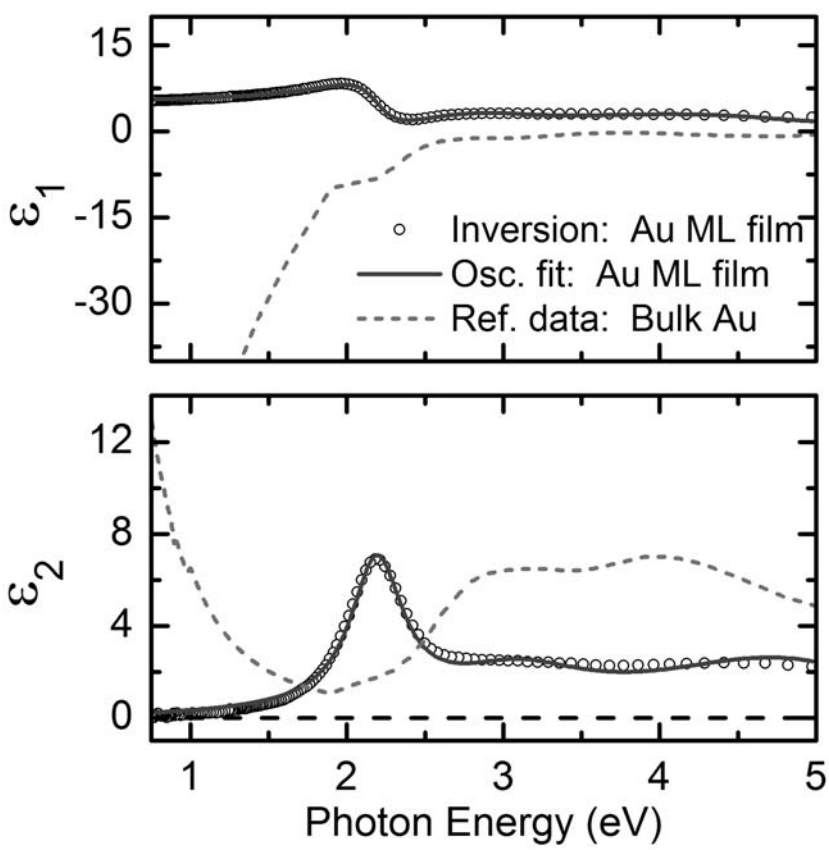

Figure 1.11: Dielectric function spectra (ε_1, ε_2) for the Au nanocrystal film prepared on a glass substrate determined from numerical inversion (open circles), parameterized fit to inversion data from Table 1.3 (solid line), and bulk Au (dashed line) all over the spectral range from 0.75 to 5.0 eV.

Table 1.3: Energy-independent parameters describing the three Lorentz oscillator model used to fit the (ε_1, ε_2) spectra obtained from artifact minimization and numerical inversion for the Au nanocrystal film on a SiO_2 slide. Also shown are the bulk film thickness (d_b) determined from fitting ellipsometric spectra in (Δ, ψ) using the (ε_1, ε_2) spectra obtained for the Au nanocrystal film deposited on native oxide covered crystalline silicon and the unweighted estimator, σ, from the parameterization of the dielectric function spectra.

D_b = 7.233 ± 0.0904 nm **σ = 0.1731**

E_0 (eV)	Γ (eV)	A (eV)	E_g (eV)	ε_∞
2.2009±0.00156	0.4071±0.00548	2.5834±0.0403	-	2.6588±0.0392
3.138±0.0219	1.098±0.0962	1.7485±0.206	-	-
4.8569±0.0377	2.0803±0.173	4.9967±0.416	-	-

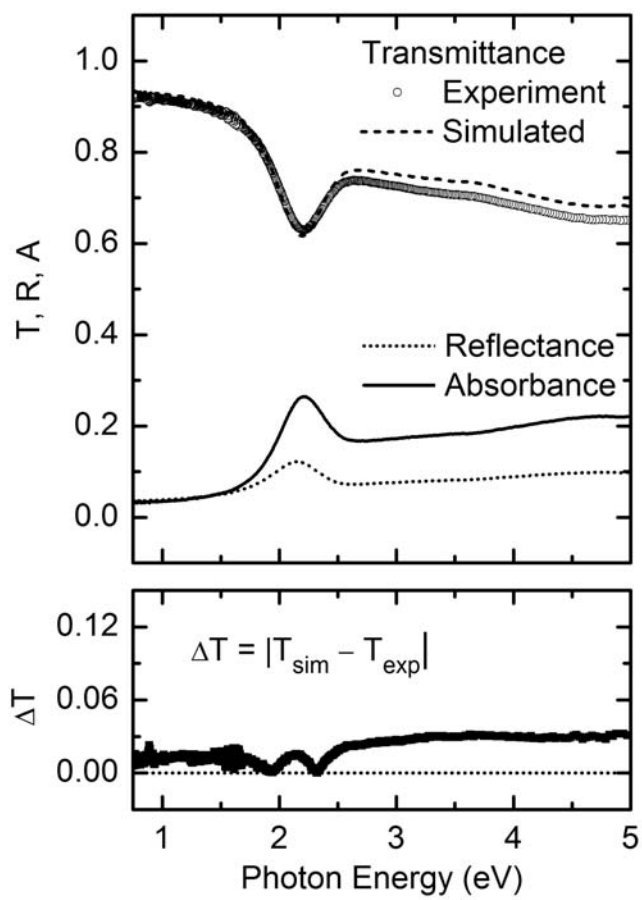

Figure 1.12: (top) Normal incidence transmittance spectra from experiment (open circles), simulated transmittance (dashed line), simulated reflectance (dotted line), and absorbance (solid line) of a (Au nanocrystal)/(silica substrate) structure over the spectral range from 0.75 to 5.0 eV; (bottom) Difference between simulated and experimental transmittance spectra.

The dielectric functions extracted from the spectroscopic ellipsometry analysis of the Au nanocrystal film on glass were then used to simulate normal incidence transmittance, reflectance, and absorbance spectra shown in Figure 1.12. A comparison between the experimental and simulated transmittance spectra shows reasonably good agreement below ~2.25 eV. Above 2.25 eV the experimental transmittance spectra is lower in magnitude than the simulation, potentially due to scattering effects.

References:

1. R.W. Collins and A.S. Ferlauto in: H.G. Tompkins and E.A. Irene (editors), *Handbook of Ellipsometry*, (William Andrew, Norwich NY, 2005).
2. D. T. F. Marple, *Phys. Rev.* **129**, 2466 – 2470 (1963).
3. J.I. Pankove, Optic*al Processes in Semiconductors*, (Dover Publications, New York, 1975).
4. J. Lee, P. I. Rovira, I. An, and R. W. Collins, *Rev. Sci. Instrum.* **69**, 1800 (1998).
5. B. D. Johs, J. A. Woollam, C. M. Herzinger, J. N. Hilfiker, R. A. Synowicki, and C.L. Bungay, *Proc. Soc. Photo-Opt. Instrum. Eng. Crit. Rev.* **72**, 29 (1999).
6. Y. Cong, I. An, K. Vedam, and R. W. Collins, *Appl. Opt.* **30**, 2692 (1991).
7. H.G. Tompkins and E.A. Irene (editors), *Handbook of Ellipsometry*, (William Andrew, Norwich NY, 2005), p. 159-171.
8. G.E. Jellison, Jr. and F.A. Modine, *Appl. Phys. Lett.* **69**, 371 (1996).
9. G.E. Jellison, Jr. and F.A. Modine, *Appl. Phys. Lett.* **69**, 2137 (1996).
10. E.D Palik (editor), *Handbook of Optical Constants of Solids*, (Academic Press, New York NY 1985), p. 293-294.

3. Admittance Spectroscopy of Thin-Film Photovoltaics

Introduction

Admittance spectroscopy has long been a routine characterization technique in semiconductor science and technology[1]. It provides information about the space charge distribution (capacitance-voltage, C-V) and the density of states distribution (capacitance-frequency, C-F) in crystalline, amorphous, and polycrystalline semiconductor materials and devices[2]. The standard understanding of admittance characterization is based on the model of a leaky flat plate capacitor. The admittance measurements conducted at different frequencies (ω), biases (V), and temperatures (T) are interpreted assuming a model where all the physical quantities (such as defect states and doping profiles) vary along one spatial coordinate perpendicular to the system electrodes. This assumption implies that the electrodes are equipotentials, so that there is no lateral current in the system. However, many practically important device structures, such as photovoltaics, have sufficiently resistive electrodes that are not equipotentials and exhibit significant currents in the lateral directions.

The purpose of this work is to introduce a theory of admittance characterization for a broad range of systems with resistive electrodes. The theory provides a practical method to effectively determine specific device parameters, such as shunt resistance, lateral resistance, non-uniformities, capacitance, and others. More specifically, we consider a distributed system exhibiting leaky photo-diode and capacitive properties, whose discrete equivalent circuit is shown in Fig. 1. The fundamental element of the system includes: 1) a photo-diode characteristic of the semiconductor material; 2) a capacitance related to the material response to an ac voltage; and 3) a shunt resistance, all in parallel with each other. This model and the theoretical development make no reference to specific material combinations. Also, we consider both one-dimensional (1D) and two-dimensional (2D) systems.

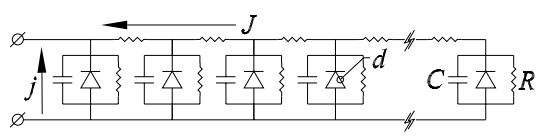

Fig. 1: Equivalent circuit of a device with a resistive electrode in the lateral direction and distributed diode, capacitance, and shunt resistance in the transverse direction.

A similar but simpler model, without distributed capacitance and shunt resistance, was analyzed earlier to describe dc operations of photovoltaics[3]. The previous work introduced a characteristic decay length, L_0, of a small electric perturbation in the lateral direction. It was shown that the decay length delineates the region in which current is collected (the active area) and, therefore, influences the *I/V* characteristics of the device. In the present work, the concept of decay length is extended to include systems with distributed shunt resistance and capacitance, resulting in two new characteristic lengths, L_R and L_C, that describe the decay of an ac perturbation in the system and determine the frequency-dependent admittance. Simultaneously, various regimes of applied dc voltage are considered. We show that an understanding of these decay lengths plays a vital role in effective device characterization.

Theory

Our methodology consists of a qualitative analysis to provide a general overview of the phenomena and to calculate estimates of the frequency-dependent admittance. Then, starting from first principles, we present a rigorous derivation of the exact results for various testing biases and device structures. Using these results, we provide a detailed description of integrity

and uniformity diagnostic techniques for thin-film photovoltaic devices with examples of practical applications.

A complete description of the decay length approach requires that we clearly define all conceivable scenarios. First of all we note the division into the regimes of geometrically large ($l >> L$) and small ($l << L$) cells, each of which can be either 1D or 2D systems. In addition, one has to discriminate between two types of electrode configurations, namely, substrate (*e.g.* CuIn(Ga)Se or a-Si:H) and superstrate (*e.g.* CdTe) devices. Therefore, there are a total of eight conceivable nominally different scenarios, with the four 1D scenarios presented in Fig. 2. A small electric perturbation at the input of the circuit in Fig. 1 will decay in the lateral direction over the characteristic length, L, determined by the electrode resistance and current leakage through the transverse resistors, diodes, and capacitors. The decay length L, together with the linear dimension of the electrode l, determine the active region of the system as shown for the various scenarios in Fig. 2.

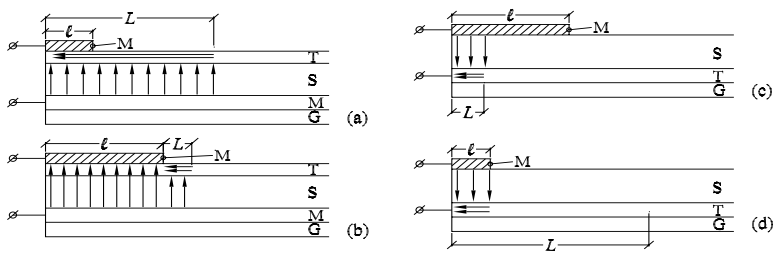

Fig. 2: Examples of four possible 1D device scenarios: (a) small, substrate; (b) large, substrate; (c) large, superstrate; and (d) small, superstrate. The device components are labeled as M, T, S, and G for metal, TCO, semiconductor, and glass, respectively. The arrows represent the active regions of current collection defined by the decay length L relative to the cell size l.

In the framework of the qualitative analysis, the characteristic decay length is estimated as the minimum of the three partial lengths, L_R, L_C, and L_d (decay length of an ac voltage due to diodes). Straightforward calculations show that $L_R = \sqrt{R/\rho}$, $L_C = \sqrt{1/(\omega c \rho)}$, and L_d depends on the applied dc bias and is related to the previously defined dc decay length, L_0. In these equations, ω is the testing frequency, R is the specific shunt resistance, ρ is the sheet resistance of the resistive electrode, and c is the specific capacitance. By applying qualitative arguments it is shown that the measured capacitance splits into high and low frequency regimes. In the low frequency regime, the capacitance is constant and depends on device parameters, while in the high frequency regime the measured capacitance is frequency dependent with $C \sim \sqrt{c/(\omega\rho)}$ for a large superstrate device.

In the rigorous derivation we provide a general formalism for calculating the frequency-dependent admittance for a broad range of devices and testing scenarios. We show that the rigorous results are similar to the qualitative results with the two frequency regimes of the measured capacitance and conductance defined by a characteristic frequency, ω_0, given as, $\omega_0 = 1/(c\rho)(1/L_0^2 + 1/L_R^2)$. Using our general formalism, we are able to provide exact results for the eight different scenarios discussed above. We show that for the cases of small superstrate cells our results reduce to the typical analysis of admittance results applied in the current standard practice, while for other types of cells there are important differences that must be considered for proper device characterization.

Practical Implications

We believe that our work introduces a diagnostic technique applicable to practically any semiconductor junction. Here we discuss in more detail the case of thin-film photovoltaics to provide examples of device parameter evaluation. For definiteness, we focus on the substrate type of photovoltaics, particularly $CuIn(Ga)Se_2$ with the typical structure (glass / metal / $CuIn(Ga)Se_2$ / CdS / buffer) and the following parameters: buffer (TCO) layer sheet resistance of $\rho \sim 10\ \Omega/\square$; current density $j_0 \sim 0.03\ \mathrm{A/cm}^2$ (for 1 sun light intensity); shunt resistance $R \sim 10^4\ \Omega{\cdot}\mathrm{cm}^2$; and capacitance $c \sim 1\ \mathrm{nF/cm}^2$. Corresponding to these parameters are the decay lengths $L_0 \sim 0.3$ cm and $L_R \sim 30$ cm, and the characteristic frequency $\omega_0 \sim 10^9$ rad/s. Note, however, that the current j_0 can be decreased and the length L_0 increased by, respectively, four and two orders of magnitude by decreasing the light intensity from 1 sun to the typical ambient room light. In addition, we assume a testing frequency range of $\omega \sim 1$ to 10^7 rad/s, corresponding to the capacitive decay length $L_C \sim 10 - 10^4$ cm.

Consider as an example a small cell of radius $a = 0.1$cm deposited as a current collection terminal on the buffer layer; the other terminal is connected to the metal electrode buried under the semiconductor. The inequalities $a \ll L_0$ and $\omega \ll \omega_0$ correspond to the low frequency regime of a 2D small cell with the conductance and capacitance given by,

$$G = \frac{2\pi}{\rho}\frac{1}{\ln(L/a)} \quad \text{and} \quad C = \frac{\pi}{\rho\omega}\frac{1}{[\ln(L/a)]^2}\arctan\left[\frac{L_0^2 L_R^2}{L_C^2\,(L_0^2 + L_R^2)}\right]. \tag{1}$$

Measuring *G* and *C* under these conditions will give information about ρ and j_0. The capacitance as a function of frequency is presented in Fig. 3.

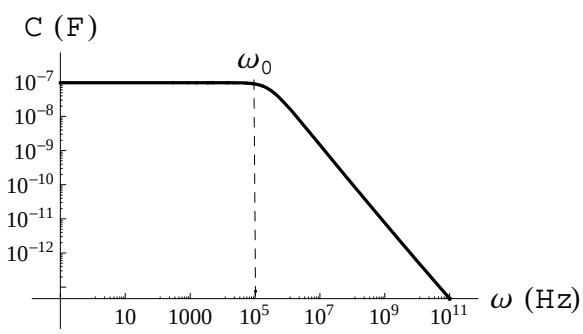

Fig. 3: Prediction of capacitance as a function of frequency for a small 2D substrate cell under the conditions discussed in the running text. The measured capacitance is constant in the region $\omega \ll \omega_0$ and goes as $1/\omega$ in the region $\omega \gg \omega_0$, where $\omega_0 \sim 10^5$ rad/s.

Also, in the low frequency regime the measured frequency-dependent capacitance will have to be attributed to the intrinsic $c(\omega)$, if any, which was considered constant our formulation, thus giving the standard admittance spectroscopy information about the material related to space charge density and defect energy spectra. We note that the typical frequency dependence for $c(\omega)$ is logarithmically weak and can hardly be mistaken for the above predicted $C \propto 1/\omega$ in the high frequency region.

Under the same conditions, decreasing the light intensity will eventually put the system into the regime where $L_R \ll L_0$ and L_R becomes the predominant (smaller) decay length. This crossover, after which *C* and *G* become independent of light intensity, will determine the shunt resistance *R*. One conceivable outcome of such experimenting is that the crossover will take place at a light intensity which is above the expected value *due to the presence of a shunt* at distance L_0 from the cell. Therefore, our proposed capacitance diagnostics have the potential of detecting shunts and their distribution in the system. Another effect of low light intensity is that the characteristic frequency will change from $\omega_0 \sim 10^9$ to 10^5 rad/s, well into the testing frequency

range (as shown in Fig. 3), which makes it possible to observe the crossover between the high and low frequency regimes, thus determining ω_0 and related parameters.

Our work also provides additional examples related to the effects of different test biases as well as methods to measure other system parameters, such as V_{oc} and ideality factor. We also detail how these diagnostic techniques can be applied to thin-film photovoltaics before the device is finished so that information related to system leakage can be determined prior to metallization.

Conclusions

In conclusion, we have developed a theory of ac response by systems of distributed diodes in parallel with resistors and capacitors connected through resistive electrodes that can represent many practical devices including photovoltaics and Schottky junctions. In particular, we have shown that:

1. There exist three lateral decay lengths related to the system diodes, shunt resistors, and capacitances respectively that determine the effective frequency-dependent lateral decay length L and describe the physics of ac response in such distributed systems;
2. The response is frequency-independent below a certain characteristic frequency, above which it strongly depends on testing frequency;
3. The 1D and 2D systems behave similarly in the large device regime, $l >> L$, where l is the device lateral dimension, while in the small device regime, $l << L$, 2D systems exhibit certain unique behavior;
4. Both the capacitance and conductance are described by closed form analytical expressions as functions of frequency and dc bias and are parametrically dependent on system material characteristics;
5. Our theoretical results establish a basis for a type of admittance characterization applicable to a wide variety of semiconductor structures including photovoltaics and Schottky junctions.

References

[1] K. Schroder, *Semiconductor Material and Device Characterization*, John Wiley, 1998.
[2] P. Blood and J. W. Orton, *The electrical characterization of semiconductors: majority carriers and electron states*, Academic Press, NY 1992.
[3] V. G. Karpov, G. Rich, A. V. Subashiev, G. Dorer, J. Appl. Phys. **89**, 4975 (2001).